Insights into recovery of multi-component shale gas by CO_2 injection: A molecular perspective

Juan Zhou [a,b], Zhehui Jin [b,*], Kai H. Luo [c,*]

[a] Center for Combustion Energy, Key Laboratory for Thermal Science and Power Engineering of Ministry of Education, Department of Energy and Power Engineering, Tsinghua University, Beijing 100084, China

[b] School of Mining and Petroleum Engineering, Department of Civil and Environmental Engineering, University of Alberta, Edmonton, Alberta T6G 1H9, Canada

[c] Department of Mechanical Engineering, University College London, Torrington Place, London WC1E 7JE, UK

*Corresponding author: Kai H. Luo

Address: Department of Mechanical Engineering, University College London, Torrington Place, London

Fax number: +44 (0)20 7388 0180

Email: K.Luo@ucl.ac.uk

*Corresponding author: Zhehui Jin

Address: School of Mining and Petroleum Engineering, Department of Civil and Environmental Engineering, University of Alberta, Edmonton

Fax number: +1 780-492-6633

Email: zhehui2@ualberta.ca

Supplemental material has been included in the submission of this paper.

Abstract

Understanding the mechanism behind shale gas recovery is of great importance for achieving optimum shale gas productivity. In this work, we use Grand Canonical Monte Carlo (GCMC) simulations to investigate the adsorption and recovery mechanisms of ternary hydrocarbon mixtures comprising methane, ethane and propane in kerogen nanopores. For the adsorption of hydrocarbon mixtures in kerogen slit pores, density distributions of each component are analyzed and the results indicate that densities of methane and ethane in the first adsorption layer increase as pressure increases, while an opposite trend is observed for propane. A stronger confinement effect is observed on the heavier hydrocarbon components, increasing the difficulty of recovery. For the recovery of the multi-component shale gas, we propose a reference recovery route with pressure drawdown and CO_2 injection combined and the recovery efficiency is compared to the condition with only pressure drawdown applied. Significant enhancement in recovery ratio for all three components is observed with the CO_2 injection and a better performance is shown on heavier components and smaller pores. An increase of 60% and 40% in propane recovery ratio is achieved in the 2-nm and 4-nm kerogen slit pores, respectively. Recovery mechanisms of pressure drawdown and CO_2 injection are investigated in detail. The pressure drawdown method recovers methane from the first adsorption layer and middle of slit pore simultaneously, while extracting ethane and propane mainly from the middle of slit pore; the recovery due to CO_2 injection mainly takes place in the adsorption layers. Pressure drawdown tends to extract the lighter components and CO_2 injection is efficient in the recovery of heavier hydrocarbons. As pore width increases, the recovery ratio of pressure drawdown increases, while that of CO_2 injection decreases. Besides, the CO_2 sequestration ratio is higher in smaller kerogen slit pores.

Keywords: GCMC simulation; Multi-component shale gas; Adsorption; Shale gas recovery; CO_2 sequestration

1. Introduction

Shale gas has attracted increasing attentions among scientists and engineers as a clean energy source with high energy efficiency and abundancy [1,2]. The U.S. Energy Information Administration (EIA) has reported that around 32% of the total estimated natural gas resources are in shale formations [3]. Shale gas is mainly composed of methane with a small fraction of ethane, propane and butane with varying compositions in various shale formations [4]. Generally, some shales produce almost exclusively methane, known as dry gas wells, while wet gas wells contain significant amounts of heavier alkanes. Wet gas recovery has gained much attention recently as the heavier hydrocarbons have higher market values than methane as feedstock for a wide variety of chemical products [5]. Despite the fact that the current techniques such as pressure drawdown using horizontal wells has made a great progress in shale gas production [6], there still remain many daunting challenges, including the low recovery efficiency in the heavier hydrocarbons and the fast-falling well productivity [7,8]. Enhanced shale gas recovery (ESGR) is proposed to stimulate the shale gas production by injecting CO_2 into shale formations after pressure drawdown. The injected CO_2 plays a role of displacing the confined hydrocarbons in shales. Significant improvement in recovery has been proven by CO_2 injection [9]. In the meantime, the depleted shale gas reservoirs with huge storage sites are often recognized as the prime candiate for permanent CO_2 sequestration [10].

Shale rocks consist of organic and inorganic matters, while the pores are mainly at nanoscale. The organic matter content is a key factor, which controls the adsorption uptake in shales [11]. Kerogen is the major constituent of organic matters in most shale formations. Over the last decade, much research has been conducted on the adsorption and recovery of methane in kerogens [12–20]. Tesson and Firoozabadi [19] studied methane adsorption in kerogen slit nanopores with different degree of surface roughness. They found that while in perfectly smooth and relatively smooth nanopores methane can form adsorption layers on the pore surfaces, in a rough kerogen nanopore, such adsorption layer disappears and methane accumulate in the middle of the pore. Cao *et al*. [13] studied the recovery of methane with CO_2 injection using GCMC simulations and found that CO_2 molecules can efficiently displace methane molecules adsorbed in the shale nanopores, while CO_2 can be sequestrated simultaneously. Contrary to the wealth of knowledge on single-component gas, methane, there are limited works on the adsorption of the heavier hydrocarbons in shales. Falk *et al*. [21] investigated the adsorption of *n*-alkanes from methane to dodecane in kerogen matrix using GCMC simulation and found that adsorption of longer *n*-alkanes is energetically more favorable. Firoozabadi and his coworkers [22–24] have systematically studied the adsorption of light hydrocarbons from methane to butane in shale samples or isolated kerogens through experiments and proposed a model for estimation of absolute adsorption based on the adsorbed layer volume. Far fewer works have been reported on recovery of the heavier hydrocarbons in shales. Wu *et al*. [25] performed a molecular dynamics (MD) simulation to study the recovery process of methane and ethane binary mixtures from 2 and 4 nm-wide nanopores driven by pressure difference. They found that the ratio of the production rate of ethane and methane from the pores is only slightly smaller than their initial mole ratio inside the pores. Bui and Akkutlu [7] simulated the recovery of quinary hydrocarbon mixture from methane to pentane by pressure drawdown using GCMC simulations. Their results indicated that recovery by the sole pressure drawdown process shows quite low efficiency as the heavier hydrocarbons are trapped in the shale reservoir, while the lighter components can be produced. The previous researches provide good guidance for the recovery of hydrocarbons, but recovery of multi-component hydrocarbons in kerogens is far from being understood. The existing research [7,25] on recovery of multicomponent hydrocarbons applies the process of pressure drawdown, which has been proven to be inefficient for the heavier hydrocarbons. Besides, simplified pore models such as the graphite slit pore model are used in these studies, which are not able to represent the complicated structures of kerogens.

In this work, we aim to investigate the adsorption of ternary hydrocarbon mixtures of methane, ethane and propane in kerogens and examine the recovery efficiency of CO_2 injection using GCMC simulations. A realistic kerogen slit-pore model is generated to represent the pore structure in organic matters [26,27]. We then analyze the adsorption of the ternary hydrocarbon mixtures in kerogen slit pores, in which the pressure and pore size effects are considered. Moreover, we discuss the adsorption of CO_2-hydrocarbon mixtures. Finally, we simulate the recovery process of multi-component hydrocarbons with pressure drawdown and CO_2 injection. Different recovery mechanisms associated with the pressure drawdown and CO_2 injection are discussed in detail. The CO_2 sequestration efficiency is also assessed.

2. Methodology

2.1. Construction of kerogen slit pores

Slit-shaped kerogen pore models are constructed to represent the organic pore structure in shales [26,27]. Type II kerogen is chosen for its high potential in producing shale gas [28–30]. The molecular model of the kerogen unit used in this work was developed by Ungerer *et al*. [31] based on experimental data reported by Kelemen *et al*. [32]. The chemical formula is $C_{242}H_{219}O_{13}N_5S_2$ and its molecular structure is illustrated in **Fig. 1a**.

To create the kerogen matrixes and slit pores, we perform series of MD simulations [33] in the canonical ensemble (NVT) and isobaric-isothermal ensemble (NPT) using the Large-scale Atomic/Molecular Massively Parallel Simulator (LAMMPS) package [34]. The intramolecular interactions of kerogen are calculated using the Dreiding force field [35]. Firstly, the initial structure of kerogen macromolecule is relaxed individually by MD in the NVT ensemble. Then, 12 relaxed kerogen units are randomly placed in a large simulation box of 10 × 10 × 10 nm^3 and NVT simulations are conducted at 900 K for 250 ps. After that, the system undergoes series of NPT simulations at a fixed pressure of 20 MPa and the temperature is stepwise decreased from 900 K to 700 K, 500 K and finally 300 K (400 ps for each temperature). The final kerogen matrixes are collected for further creation of kerogen slit pores by extending the simulation box in the Z-direction as shown in **Fig. 1b** [18]. The pore width *W* is defined as the distance between the very last atoms from each kerogen surface in the Z-direction. Two pore widths of 2 nm and 4 nm are constructed to investigate the pore size effects. In the computational configuration (Fig. 1b), the slab geometry is periodic in the X- and Y-directions while that in the Z-direction is nonperiodic. The use of the conventional three-dimensional Ewald summation technique might incur undesirable long-range electrostatic interactions in the Z-direction. Thus, an empty space is inserted between the periodic replicas in the Z-direction, which is large enough to ensure that the long-range electrostatic interaction in that direction does not alter the fluid distributions [36]. Tests are conducted to ensure the length of empty space is sufficient so that the artificial effects are eliminated. During the GCMC simulations, the movement of gas molecules is restricted within the kerogen slit pore, but not into the vacuum.

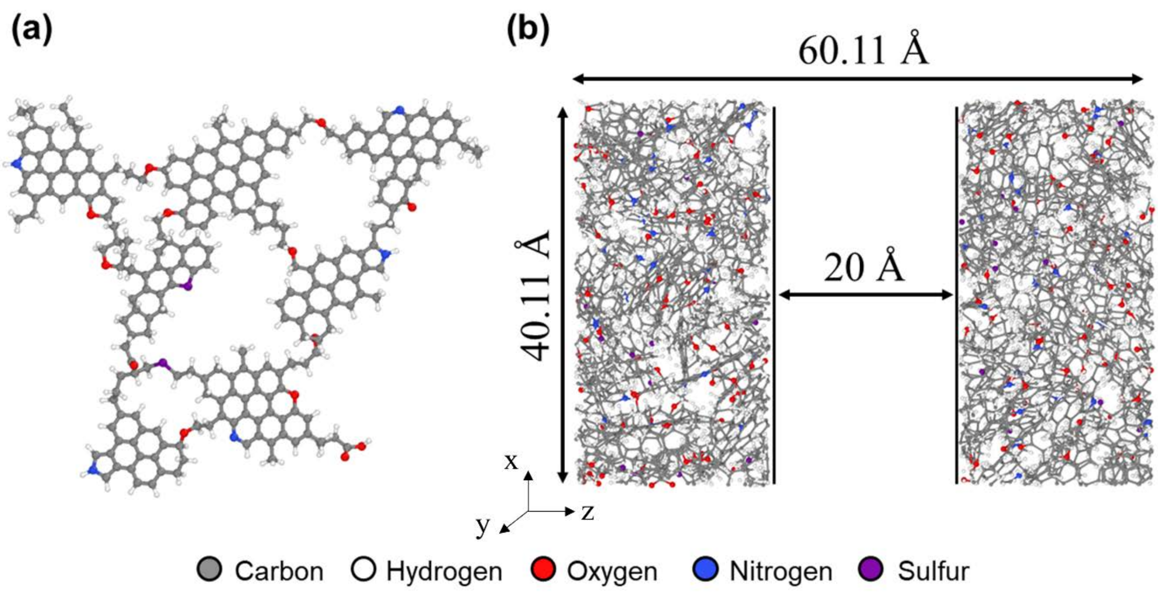

Fig. 1. (a) Molecular model of type II-C kerogen. (b) Molecular model of kerogen slit nanopore. The pore width is 2 nm. Carbon atoms are depicted by gray balls, hydrogen by white, oxygen by red, nitrogen by blue, and sulfur by purple.

2.2. Force field

Three hydrocarbons including methane, ethane, and propane, are considered in this work as the much heavier hydrocarbons (C_{4+}) only make up a very small proportion in the shale gas. The composition of the hydrocarbon mixtures studied in this work is listed in **Table 1**, which is based on the shale gas composition produced from the Mississippian Barnett Shales of the Fort Worth Basins, Texas [37]. The Barnett Shale is known as an organic-rich, type II marine shale and has been proven to have an enormous gas storage capacity and good potential for long-term production [30].

Table 1 Composition of the shale gas mixture

Molecular Weight	**Mole fraction**		
	CH_4	C_2H_6	C_3H_8
19.55	0.80	0.15	0.05

The TraPPE force field [38] is adopted for alkanes and the United-Atom models are employed. The Lennard Jones parameters for interactions between like pseudoatoms are summarized in **Table 2**. Lorentz-Bertherlot mixing rules [39] are employed to calculate unlike interactions. A cutoff of 14 Å is applied for short-range Lennard-Jones interactions with analytical tail corrections [40]. The bond length between pseudoatoms in C_2H_6 and C_3H_8 is fixed as 1.54 Å. The bond bending potential is calculated by a harmonic relationship,

$$u_{bend}(\theta) = \frac{k_\theta}{2}(\theta - \theta_0)^2, \qquad (1)$$

where the force constant k_θ / k_B is 62500 K rad^{-2} [41], k_B is the Boltzmann constant. The equilibrium angle θ_0 is 114°. CO_2 molecules are described with a rigid model [42]. The nonbonded parameters are listed in **Table 2**. The length of the C-O bond and the bond bending angle of O-C-O are fixed as 1.16

Å and 180°, respectively.

Table 2 Lennard-Jones parameters and partial charges used for hydrocarbon and CO_2 molecules [38,42]

(Pseudo)atom	**ε/k_B (K)**	**σ (Å)**	**q (e)**
CH_4	148.0	3.73	0.00
CH_3-	98.0	3.75	0.00
-CH_2-	46.0	3.95	0.00
C-CO_2	27.0	2.80	0.70
O-CO_2	79.0	3.05	-0.35

2.3. GCMC simulation

Adsorption of the hydrocarbons and CO_2 is investigated through GCMC simulations in the grand canonical ensemble (μVT) using MCCCS Towhee code [43]. During the simulations, the coordinates of the atoms in kerogen are fixed and GCMC moves are only applied to the gas molecules, including insertion, deletion and translational moves. For ethane, propane and CO_2 molecules, rotational moves are also performed. The fluids confined within the kerogen nanopores are assumed to be in chemical equilibrium with the external bulk fluids, which can be considered as those residing in the natural fracture or microcracks in shales. Besides, the pressure throughout the simulations refers to that of the external bulk reservoir. Values of chemical potential are calculated by the Widom's insertion method [44,45] using Monte Carlo simulations in the NVT ensemble, where the fluids are simulated in bulk phase. Density of bulk mixtures as a function of pressure and temperature is calculated by the Peng−Robinson equation of state (PR-EOS) [46].

3. Results and Discussion

In this section, we first investigate the adsorption of methane, ethane and propane ternary mixtures in kerogen slit pores either in the absence or presence of CO_2. Then, the recovery mechanisms of hydrocarbons are analyzed and we further discuss the practical implications for shale gas recovery and CO_2 sequestration.

3.1. Adsorption of hydrocarbons in kerogens

The density profiles of methane, ethane and propane in different kerogen nanopores at various pressures at 338.15 K are presented in **Fig. 2**. The results indicate that a strong first adsorption layer forms near the kerogen surface for all pressures and the second adsorption layer is pronounced at pressures higher than 10 MPa. Near the kerogen surface, the methane density in the first adsorption layer increases with increasing pressure, while that of propane decreases. At low pressures, the adsorption sites on the kerogen surface are not completely occupied and the interaction between propane and kerogen is stronger than the other two components [21], so propane can occupy more adsorption sites. As pressure increases, the adsorption sites are almost filled up and the entropic effects become more significant, thus the propane density decreases. As an intermediate component, the increase in ethane density is less obvious. Similar phenomena have been reported in the adsorption of hydrocarbons in zeolite [47]. In the middle of pores, the density of each component increases with pressure. Besides, the density in the 4-nm slit is lower than that of 2-nm slit pore due to weaker fluid-surface interactions. It should be also noted that the first adsorption layers near the two surfaces are not symmetric and the hydrocarbon densities are non-zero on the slit pore surfaces. This is because a complex kerogen matrix is used in this work in which the surfaces are rough. Similar results have been reported in the literatures [14,19]. To further verify the effect of surface roughness on gas adsorption, we calculated the gas adsorption on a slit pore with smooth surfaces using Steele's 10-4-3 potential [48]. More details are provided in the **Supplementary material** and the hydrocarbon density distributions in the smooth graphite slit pore are plotted in Fig. S1. The first and second adsorption layers show symmetric density profiles and are more easily distinguishable compared to those in rough kerogen slit pores.

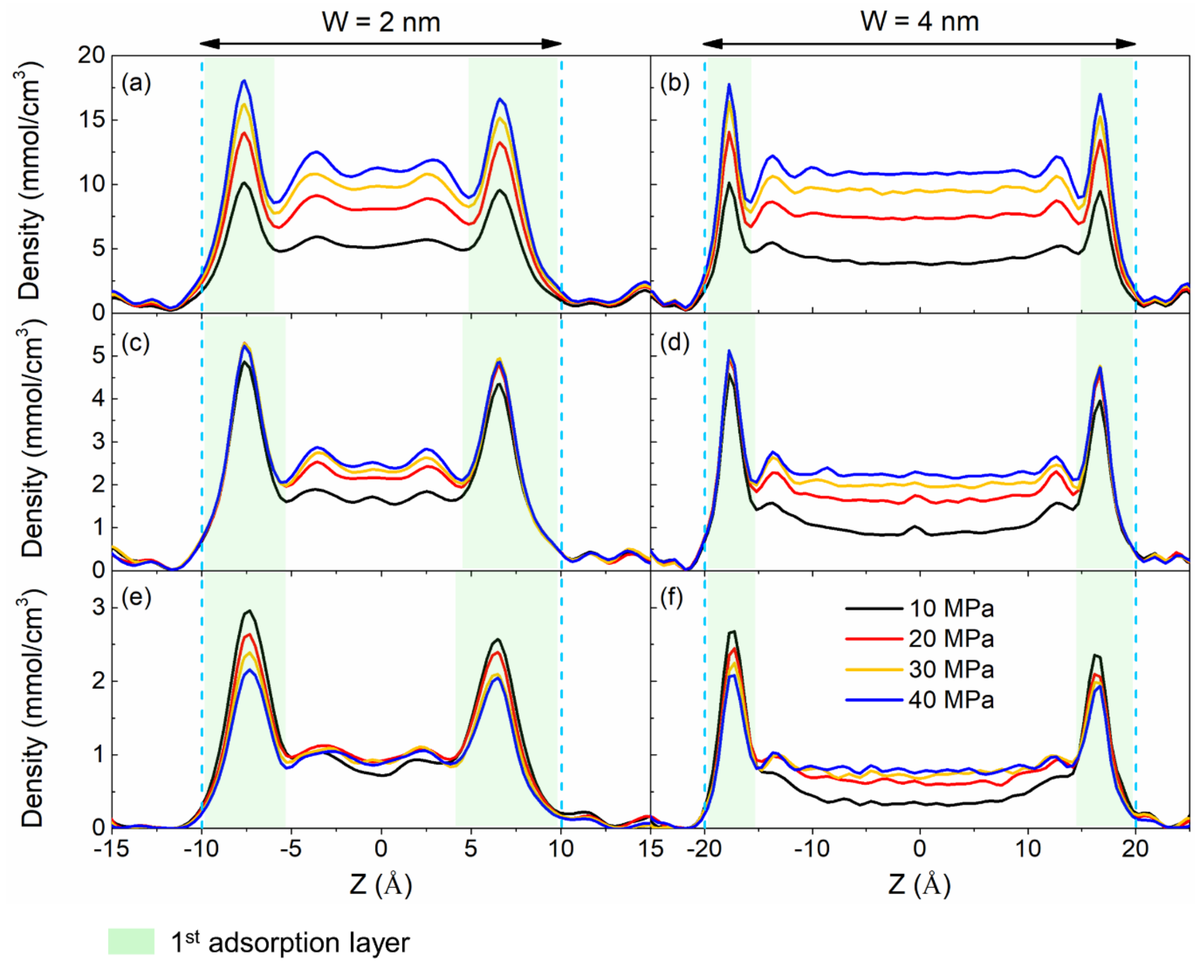

Fig. 2. Density distributions of the hydrocarbons in kerogen slit pores of different widths: (left) *W* = 2 nm and (right) *W* = 4 nm under different pressures at T = 338.15 K.

Figure 3 shows the total uptake of each component at 338.15 K in kerogen slit pores of different pore widths. The average density of component i in kerogen slit pore can be given as,

$$\rho_{ave,i} = \frac{\langle N_i \rangle}{V \cdot N_A}, \tag{2}$$

where $\langle N_i \rangle$ is the ensemble averaged number of component i in kerogen slit pores, *V* denotes the volume of the slit pore, and N_A is the Avogadro constant. Only the hydrocarbon molecules within the slit pores are considered, while those inside kerogen matrixes excluded. The average density in 4-nm kerogen slit pore is lower than that in the 2-nm kerogen slit pore, especially at lower pressures, which is mainly attributed to the difference in density distributions in the middle of kerogen slit pores. For methane and ethane, the average densities in 2 and 4-nm slit pores both increase with pressure. However, the average density of propane in 2-nm slit pore decreases, while increases in the 4-nm kerogen slit pore as pressure increases. As discussed earlier, the density of propane decreases in the first adsorption layer and increases in the middle of kerogen slit pore with increasing pressure. In the 4-nm slit pore, the middle region makes up a larger fraction and the increase in density is large enough to compensate the decrease in the adsorption layer.

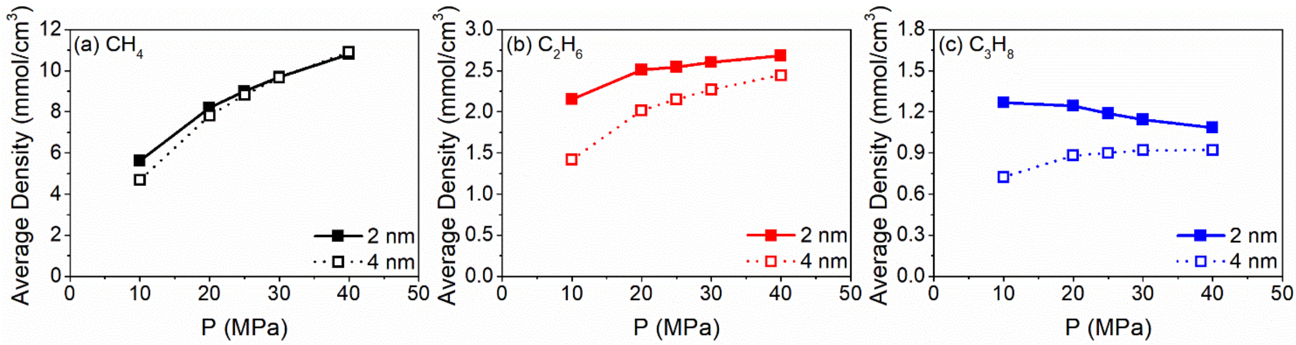

Fig. 3. Average density of hydrocarbons confined in kerogen slit pores with different pore widths: (solid) $W = 2$ nm and (dashed) $W = 4$ nm at T = 338.15 K.

To assess the confinement effect on the different types of hydrocarbons, a parameter is introduced as Confinement Effect (CE), or Enhancement Factor, defined as the ratio of molar fraction inside the pore to that in the bulk fluid for component i [7],

$$CE_i = \frac{y_{i,pore}}{y_{i,bulk}}, \quad (3)$$

where $y_{i,pore}$ and $y_{i,bulk}$ denote the molar fraction of component i within kerogen slit pores and in the bulk fluid, respectively. The values of confinement effect for each component are shown in **Fig. 4a**. The largest confinement effect is observed on propane. Both the CE values of ethane and propane are larger than one, while that of methane is smaller than one, indicating that the adsorption of the heavier component in kerogen nanopores is more favorable. As the pore width is increased to 4 nm, the confinement effect for the three components becomes less significant and the values of CE approach unity. With increasing pressure, the CE values also get close to unity. At higher pressures, the confined space is more densely packed, the difference between molecule types becomes less significant [49]. To further explain the confinement effect on different hydrocarbons, we calculate the distributions of CE values within the slit pore along Z-direction (**Fig. 4b**). Confinement effect of heavier components, such as ethane and propane, is obviously higher in the region close to the kerogen surfaces. Lighter component, methane, is forced to stay in the middle of the slit pore where the interaction from the kerogen surfaces is weaker.

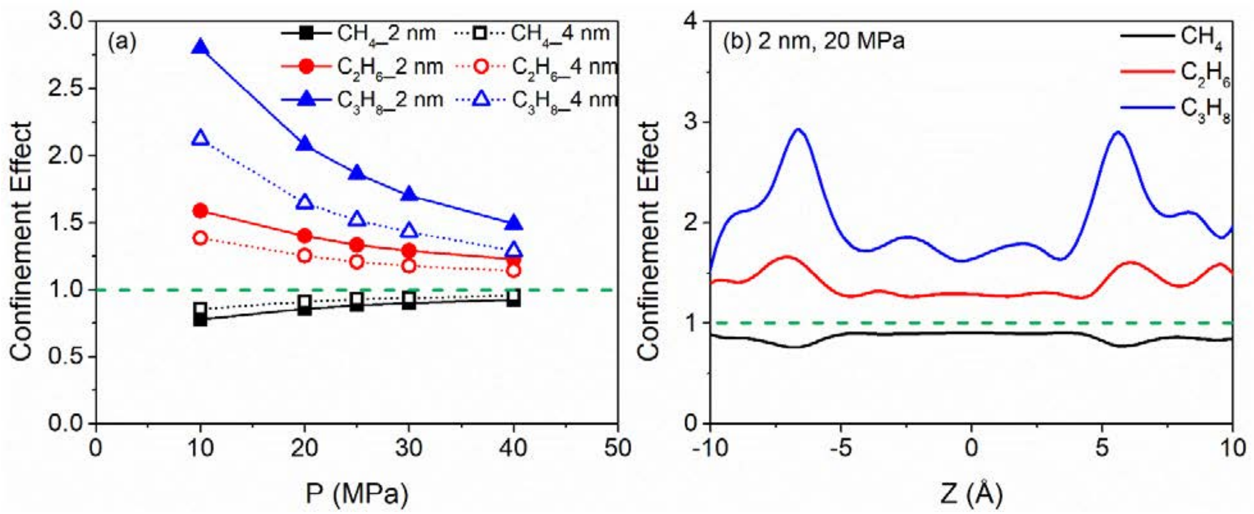

Fig. 4. (a) The ratio of molar fraction inside the pore with that in the bulk phase (noted as Confinement Effect) for each component in kerogen slit pores with different pore widths: (solid) W = 2 nm and (dashed) W = 4 nm at T = 338.15 K. (b) Distribution of CE values in the 2-nm kerogen slit pore along Z direction at P = 20 MPa and T = 338.15 K.

3.2. Adsorption of CO_2-hydrocarbons mixtures in kerogens

The density distributions of CO_2 and hydrocarbons mixtures with a bulk mole fraction of $y_{CO_2} = 0.2$ at 338.15 K and over a range of pressures from 12.5 to 45 MPa in 2-nm kerogen slit pores are presented in **Fig. 5**. The mole fractions within the hydrocarbons are fixed at 0.8, 0.15, 0.05 for methane, ethane and propane, respectively. Similar to the adsorption of hydrocarbons in the absence of CO_2, the density in the middle of kerogen slit pores increases as pressure increases. In the first adsorption layers, the density of methane, ethane and CO_2 increases with increasing pressure, while the opposite is true for propane. **Fig. 6** presents the density distributions in 4-nm kerogen slit pores.

Similar trends in the density distribution can be observed as in the 2-nm kerogen slit pores. Besides, for all the components, the density in the middle of kerogen slit pores is lower than that of 2-nm kerogen slit pores due to the weaker fluid-surface interactions.

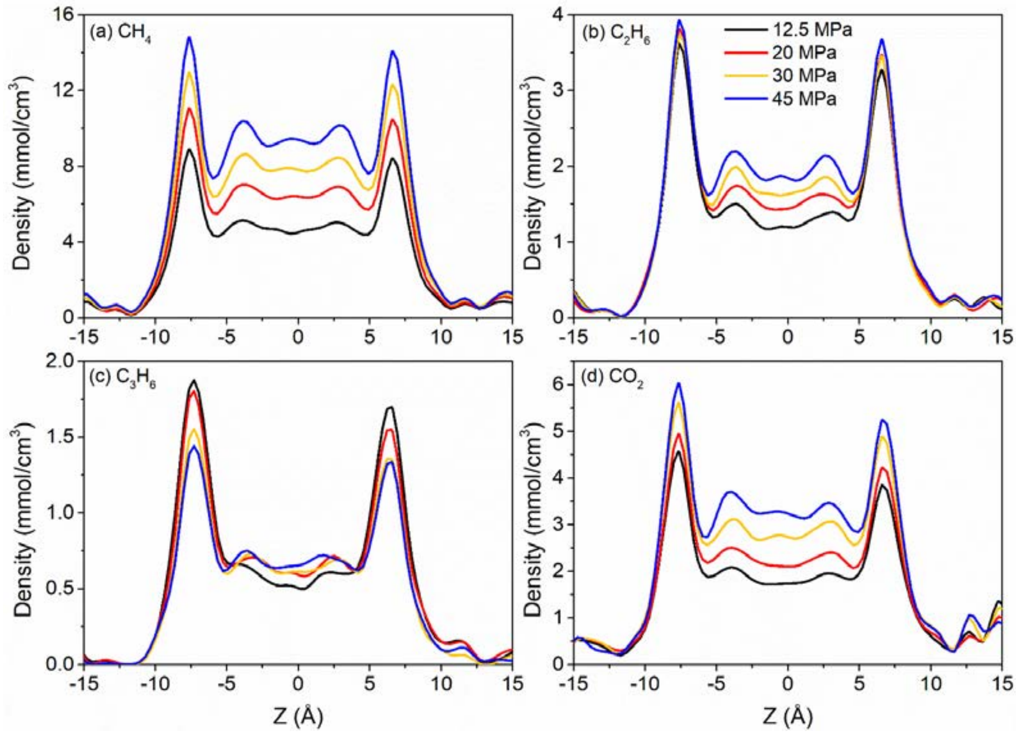

Fig. 5. Density distributions of hydrocarbons and CO_2 in 2-nm kerogen slit pores under different pressures at T = 338.15 K. Mole fraction of CO_2 is $y_{CO_2} = 0.2$. Results of mixtures with a mole fraction of $y_{CO_2} = 0.4$ are presented in **Fig. S2**.

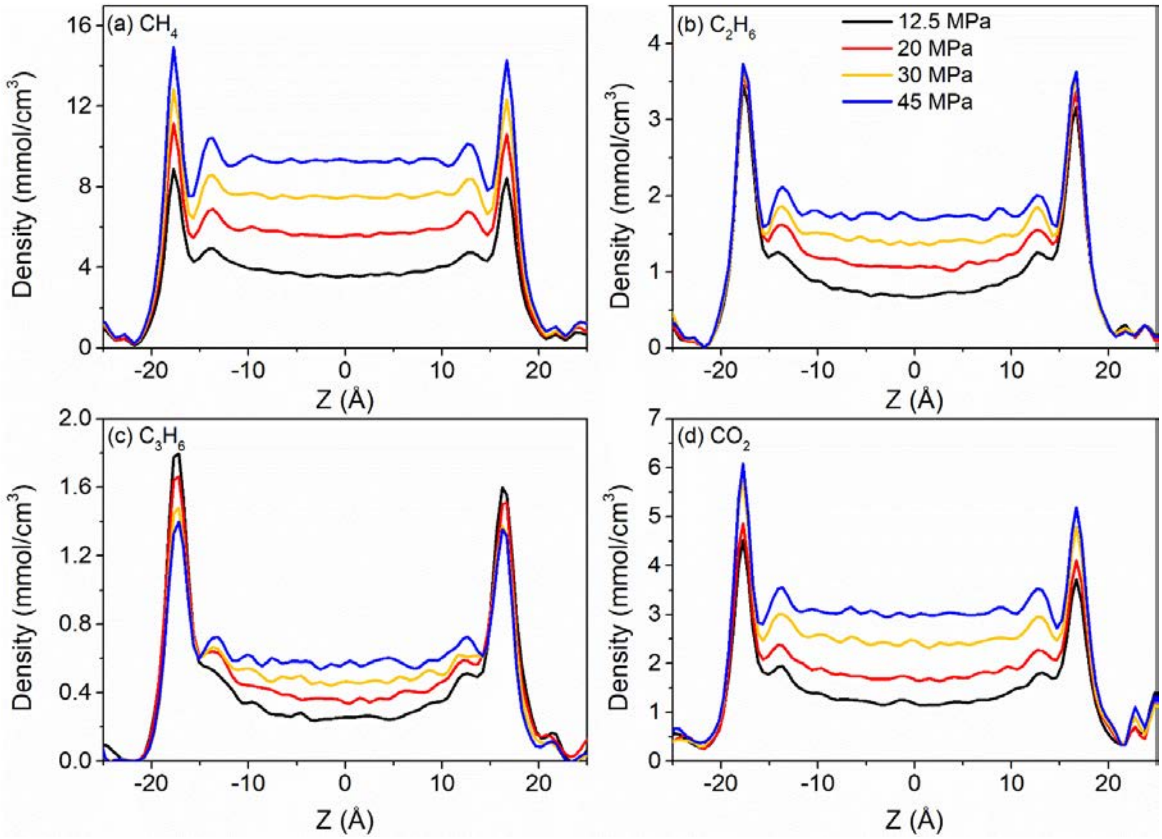

Fig. 6. Density distributions of hydrocarbons and CO_2 in 4-nm kerogen slit pores under different pressures at T = 338.15 K. Mole fraction of CO_2 is $y_{CO_2} = 0.2$. Results of mixtures with a mole fraction of $y_{CO_2} = 0.4$ are presented in **Fig. S3**.

3.3. Recovery of hydrocarbons from kerogen slit nanopores

To explore the mechanisms of shale gas recovery by pressure drawdown and CO_2 injection and assess the efficiency of shale gas recovery and CO_2 sequestration, a simplified recovery process is proposed as shown in **Fig. 7**. A typical shale gas reservoir condition with the initial pressure of 40 MPa is considered in this work. After the primary pressure drawdown stage, the reservoir pressure is reduced to 25 MPa and then two successive CO_2 huff-n-puff cycles are performed as in our recent work [18]. One CO_2 huff-n-puff cycle is achieved by first injecting CO_2 into the shale gas reservoirs and then applying a pressure drawdown process after the system has reached equilibrium [50,51]. Here GCMC simulations instead of MD simulations are conducted to obtain the equilibrium properties of hydrocarbon mixtures and CO_2 in kerogen nanopores. Takbiri-Borujeni et al. [52] used MD simulations to simulate the CO_2 huff-n-puff process for dodecane recovery. Compared with MD simulation, GCMC simulations are computationally less expensive to study the equilibrium properties. During the CO_2 injection process, we assume that the pore volume in the macropores and fractures, which is connected to the nanopores, remains the same. Therefore, the individual hydrocarbon density in the bulk phase of the $CH_4/C_2H_6/C_3H_8/CO_2$ mixture is the same as that in the bulk $CH_4/C_2H_6/C_3H_8$ mixture during CO_2 injection. The pressure of the bulk $CH_4/C_2H_6/C_3H_8/CO_2$ mixture after the CO_2 injection can be determined by the molar fraction and hydrocarbon density in the mixtures by using PR-EOS [46]. The composition of the confined fluids in kerogen slit pores is recorded in the equilibrium state after every production stage. We assume that the dynamics-transport resistances are not considered during the fluids flow from the kerogen nanopores [7].

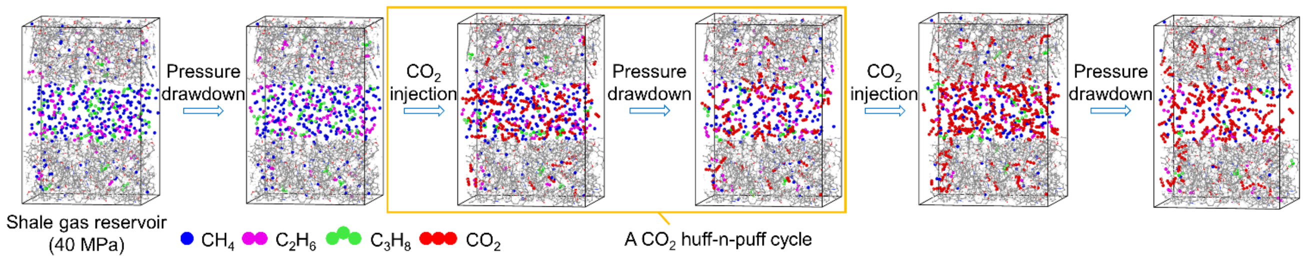

Fig. 7. Schematic representation of shale gas recovery process. More information about the recovery process is provided in **Supplementary material**.

Evolution in the average densities of each component in the 2-nm kerogen slit pores during the whole shale gas recovery process is presented in **Fig. 8**. During the shale gas recovery process, the methane and ethane molecules are released continuously both in the pressure drawdown and CO_2 injection stages (**Figs. 8a-b**). The performance of pressure drawdown seems more effective for methane, while CO_2 injection performs better on ethane. It should be noted that propane is not released from the nanopores during the pressure drawdown process, but can only be recovered by CO_2 injection (**Fig. 8c**). As pressure declines, the injected CO_2 molecules are released together with the recovered shale gas (**Fig. 8d**). For W = 4 nm, the average densities of each component during the recovery process is shown in **Fig. 9**. In contrast to the results in 2-nm kerogen slit pores, propane molecules are found to be recovered during the pressure drawdown process despite the lower efficiency compared to CO_2 injection.

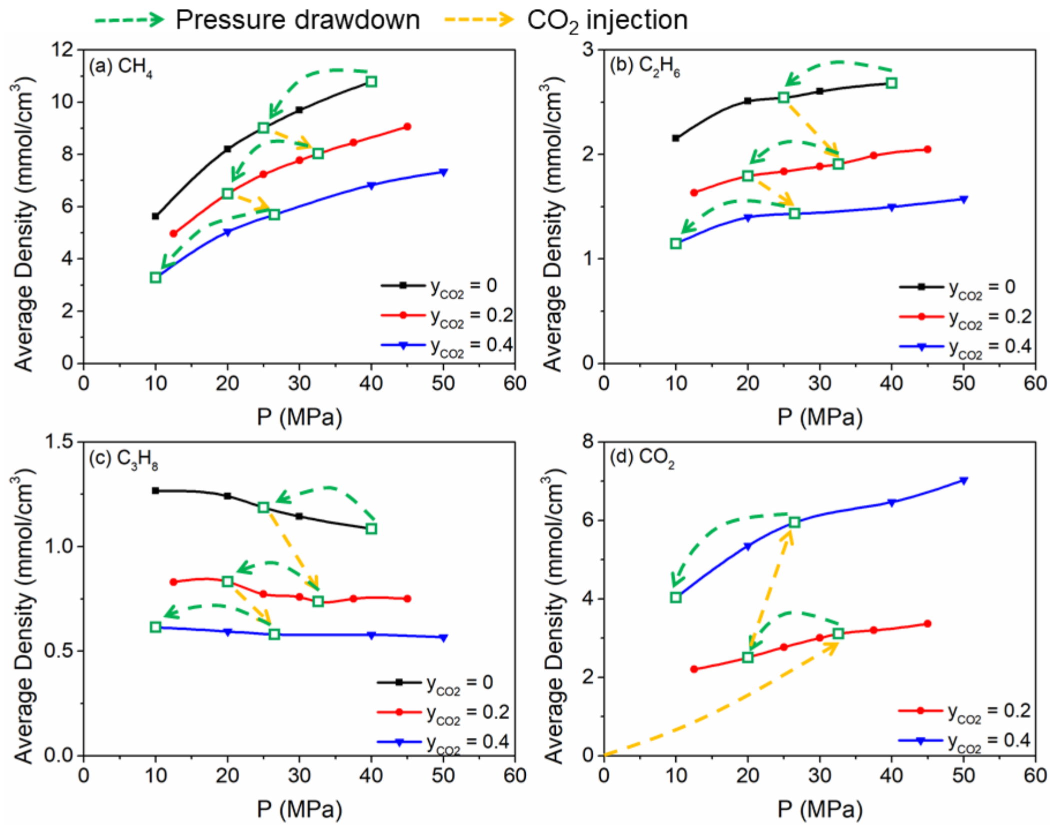

Fig. 8. The average densities of each component in the 2-nm kerogen slit pores during the shale gas recovery process. The arrows in the figure indicate the direction of the recovery process.

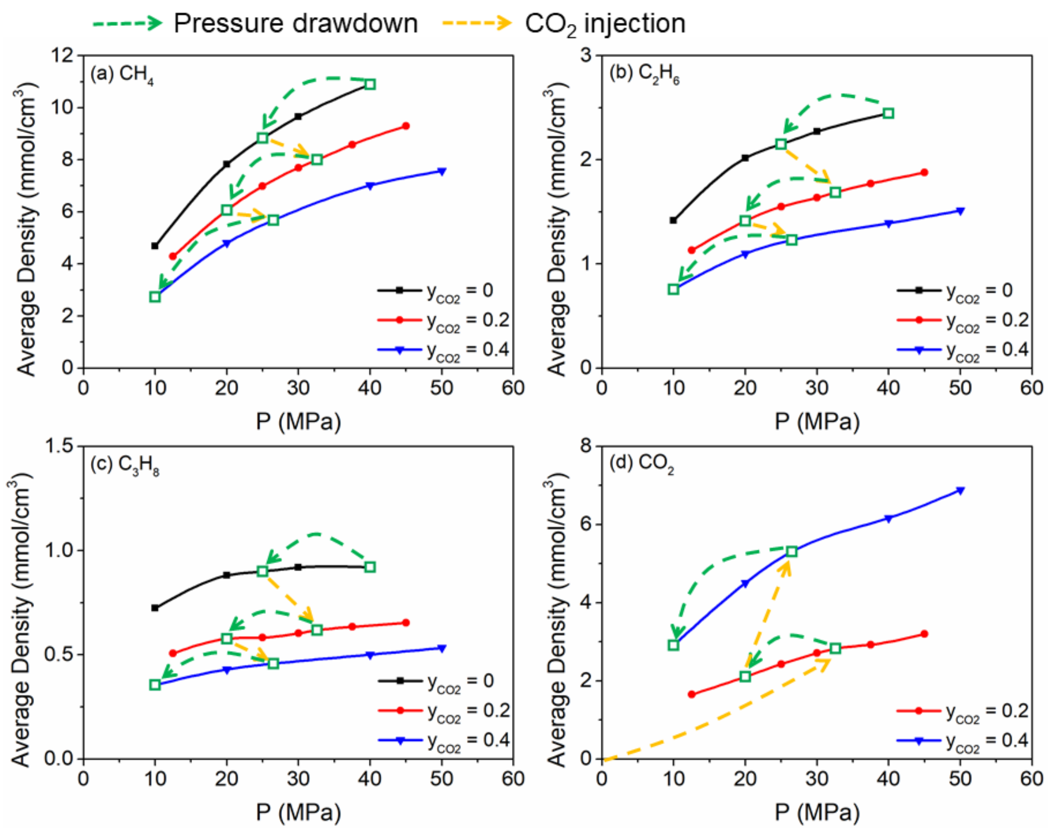

Fig. 9. The same as **Fig. 8**, but for 4-nm kerogen slit pores.

In order to quantify the recovery efficiency of pressure drawdown and CO_2 injection stages, we define the recovery ratio η_i as the ratio of the molar density of molecules released during a single stage to the initial molar density in the kerogen slit pore under 40 MPa before production, which is given as [14,53,54],

$$\eta_i = \frac{n_i^{\text{released}}}{n_i^{\text{initial}}} \times 100\%, \tag{4}$$

where n_i^{released} is the molar density of component i recovered from the kerogen slit pore, n_i^{initial} is the initial molar density of component i in the kerogen slit pore at 40 MPa before production. The calculated recovery ratios of each component for the five stages in 2 and 4-nm kerogen slit pores are presented in **Fig. 10**. In the 2-nm kerogen slit pores (**Fig. 10a**), it can be seen that for methane, the recovery ratio of pressure drawdown is higher than that of CO_2 injection. For the propane molecules, the recovery ratio has negative values during the pressure drawdown, indicating that there is no propane released at during that stage, while even some extra propane molecules are adsorbed into the nanopores. However, the CO_2 injection can recover the propane efficiently. In the case of the intermediate component, ethane, the pressure drawdown stages have relatively lower but positive recovery ratios, compared to the CO_2 injection processes. The third pressure drawdown stage has the largest recovery ratio among all the pressure drawdown processes, which can be attributed to the largest depletion in pressure. In 4-nm kerogen slit pores (**Fig. 10b**), the propane molecules are released during the pressure drawdown processes although the recovery ratio is relatively low. For methane and ethane, slight increases in recovery efficiency of pressure drawdown are found with the increased pore width, while the recovery ratio of CO_2 injection slightly decreases. In addition, among the three pressure drawdown processes, the third one achieves the highest recovery ratio. According to Figs. 8-9, the average densities of hydrocarbons increase rapidly with pressure at low pressure conditions and then increase slowly at high pressures. During the implementation of the three pressure drawdown processes, the pressure continues to decline. The hydrocarbons are slowly released at the beginning (high pressure) and then rapidly as the pressure further declines. On the other hand, the three pressure drawdown processes have different pressure declines of 15, 12.6 and 16.5 MPa for the first, second and third process, respectively (see Table S1). The largest pressure decrease is achieved in the third pressure drawdown process, which also contributes to the higher recovery ratio.

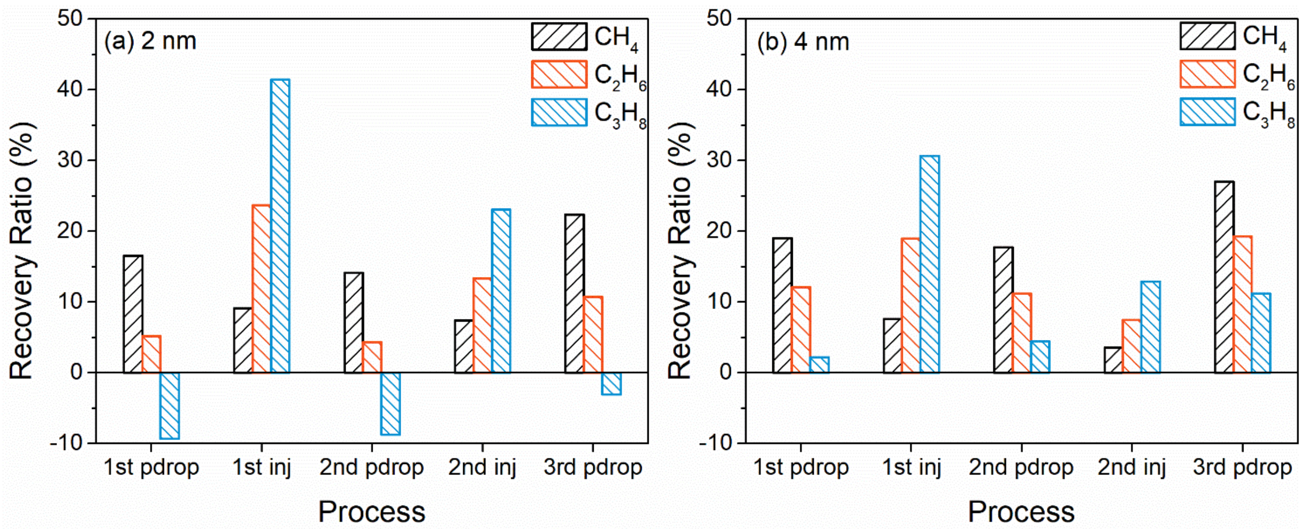

Fig. 10. The shale gas recovery ratio in the (a) 2-nm and (b) 4-nm kerogen slit pores during the gas recovery process.

Fig. 11a shows the total recovery ratios of each component in the presence of CO_2 injection. The lightest component, methane has the highest recovery ratio of 69.6% in the 2-nm kerogen slit pores and 74.9% in 4-nm pores, indicating that the lighter components are preferentially recovered. For three hydrocarbon components, the total recovery ratio of in the 4-nm kerogen slit pore is higher than that in the 2-nm kerogen slit pore. This indicates that the increase in recovery ratio of pressure drawdown is larger than the decrease of CO_2 injection. To clarify the role of CO_2 injection in the recovery process, we calculate the recovery ratio of the process with pressure drawdown only from 40 MPa to 10 MPa. The recovery ratios between the two processes are compared (**Fig. S4**). Pressure drawdown mainly releases the lighter components, such as methane and ethane, but is inefficient for the heavier component, especially in the small pores. The enhancement in recovery ratio due to CO_2 injection is also illustrated in **Fig. 11a**. The injected CO_2 significantly enhances the shale gas recovery over all three components. The largest increases around 60% and 40% are observed for propane in the 2-nm and 4-nm kerogen slit pores, respectively.

The CO_2 sequestration ratios during the recovery process are plotted in **Fig. 11b**. The CO_2 sequestration ratio is defined as the molar density of CO_2 molecules sequestrated relative to its molar density in the kerogen slit pores under the initial pressure of the reservoir, namely the maximum molar density of CO_2 sequestration in a 40 MPa reservoir, calculated by,

$$\xi_i = \frac{n_{CO_2}^{\text{sequestrated}}}{n_{CO_2}^{\max}} \times 100\% , \tag{5}$$

where $n_{CO_2}^{\text{sequestrated}}$ is the molar density of CO_2 sequestrated in the kerogen slit pore, $n_{CO_2}^{\max}$ is the maximum molar density of CO_2 in the kerogen slit pore at 40 MPa. The CO_2 sequestration ratio can be used to describe the extent of CO_2 sequestration. The CO_2 sequestration ratio is increased once the

CO_2 molecules are injected and decreased when the pressure drops. Final sequestration ratios of 21.0% and 14.9% are realized in the 2-nm and 4-nm kerogen slit pores, respectively. Higher CO_2 sequestration ratio in the 2-nm kerogen slit pore results from the stronger CO_2-wall interaction in the narrower kerogen slit pores.

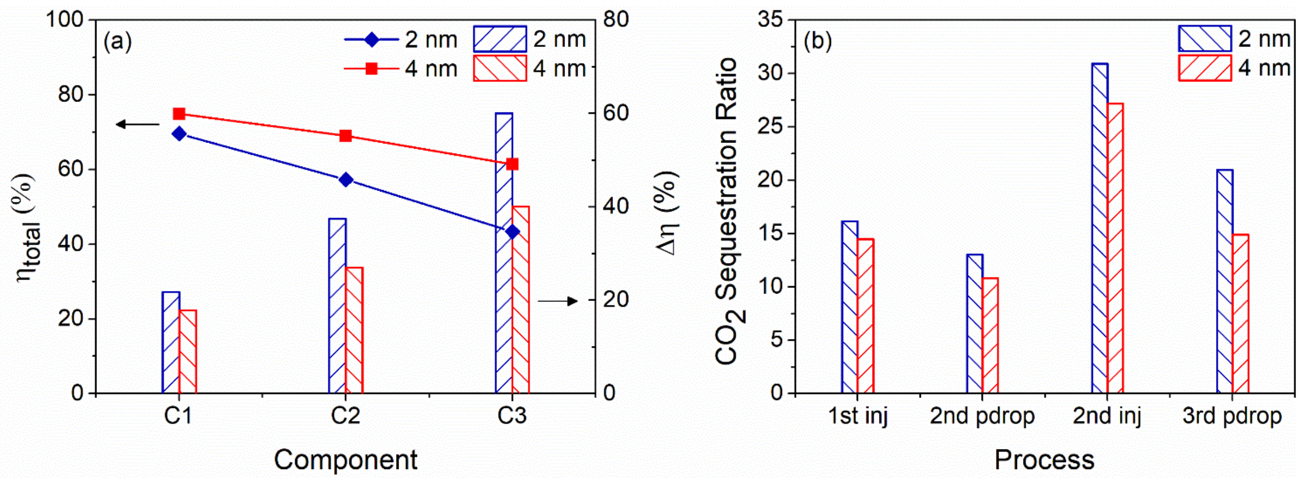

Fig. 11. (a) Total shale gas recovery ratio, η_{total}, in the presence of CO_2 injection (left y-axis) and enhanced shale gas recovery ratio, $\Delta\eta$, caused by the participation of CO_2 injection (right y-axis). (b) the CO_2 sequestration ratio in the 2-nm and 4-nm kerogen slit pores during the gas recovery process.

In order to better illustrate the underlying mechanism during the shale gas recovery, the evolution of the density distributions is studied. In 2-nm kerogen slit pores, during the pressure drawdown process, methane molecules are recovered simultaneously from both the adsorption layers and the middle of nanopores; CO_2 injection mainly recovers the methane from the adsorption layer (**Fig. 12a**). For ethane, the pressure drawdown only recovers the molecules in the middle of nanopores, while recovery by CO_2 injection takes place in both the adsorption layers and the middle of nanopores, especially in the adsorption layer (**Fig. 12b**). For propane, recovery by CO_2 injection is similar to the case of ethane. However, as pressure drops, the propane density in the first adsorption layer increases and only a very small portion in the middle of kerogen slit pore is recovered (**Fig. 12c**). Besides, CO_2 can form strong adsorption layers near the kerogen surface after injection (**Fig. 12d**).

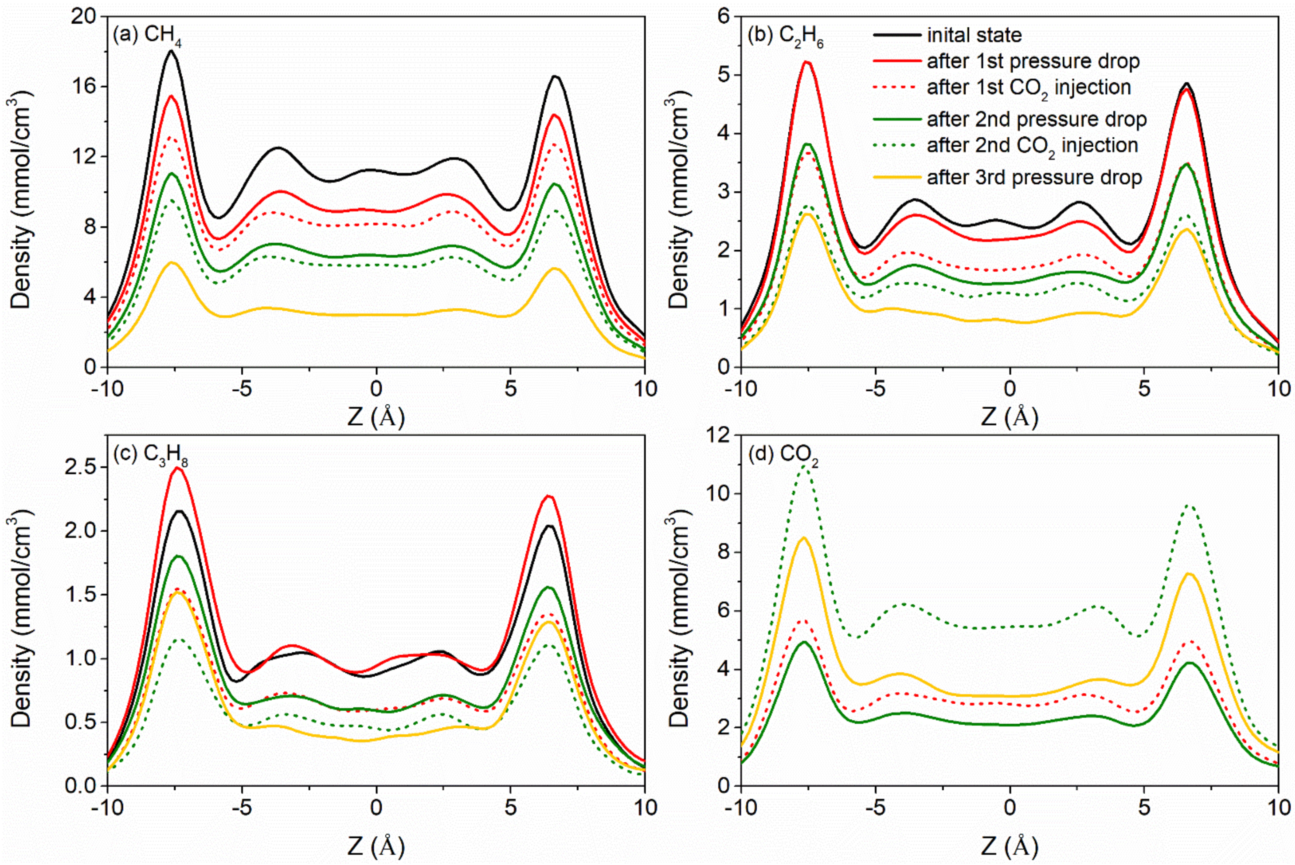

Fig. 12. Evolution of each component density distributions inside the 2-nm kerogen slit pores during the gas recovery process.

The evolution of density distributions inside the 4-nm kerogen slit pores is presented in **Fig. 13**. In 4-nm kerogen slit pores, similar recovery mechanisms as in the 2-nm kerogen slit pores are observed. Moreover, the recovery ratio of pressure drawdown increases in the middle of kerogen slit pores. Due to the weaker fluid-surface interactions in the 4-nm pores, fewer CO_2 molecules occupy in the middle of kerogen slit pores, therefore, the recovery ratio of CO_2 injection is reduced. Overall, the increase in recovery ratio of pressure drawdown is larger than the decrease of CO_2 injection, thus, the total recovery ratio increases in the 4-nm kerogen slit pores.

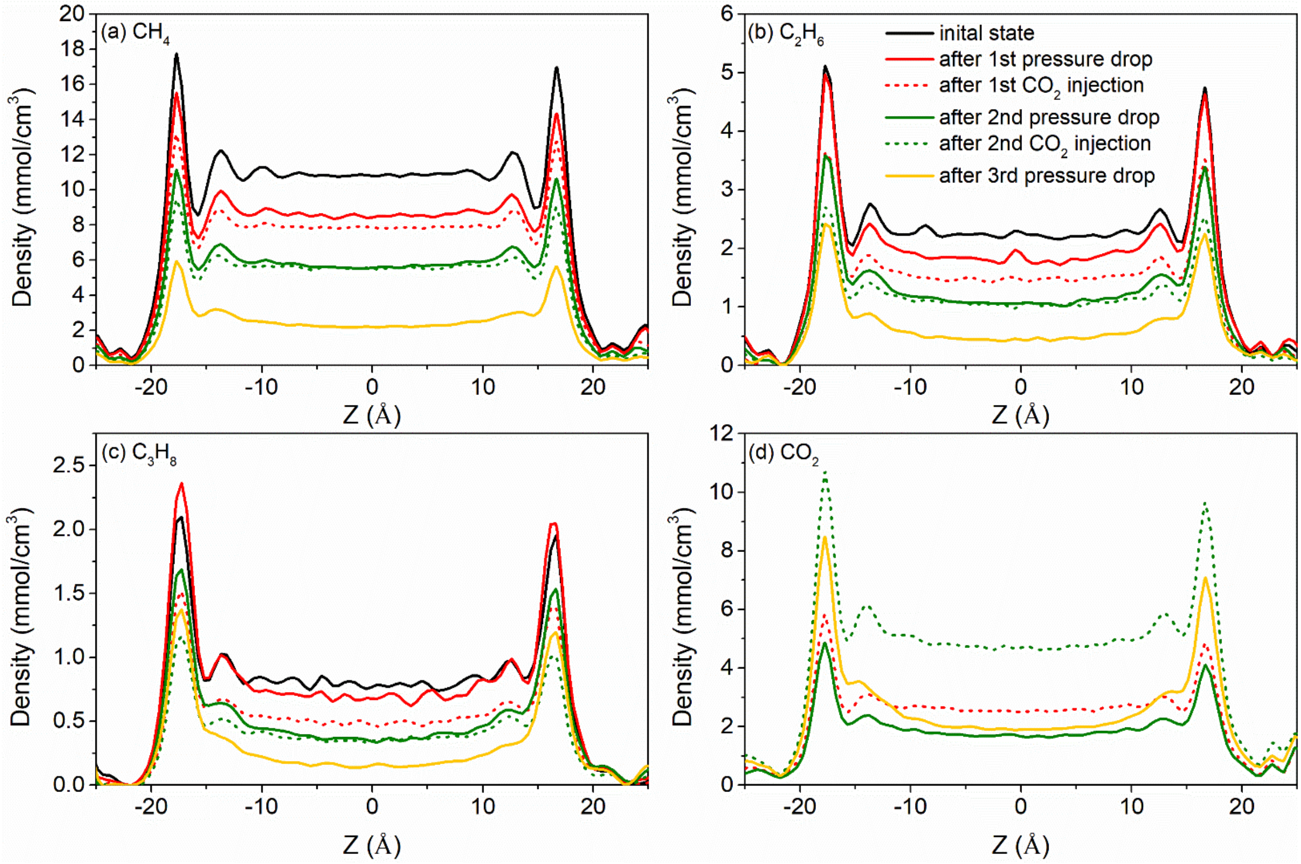

Fig. 13. Evolution of each component density distributions inside the 4-nm kerogen slit pores during the gas recovery process.

4. Conclusions

In this work, the adsorption of multicomponent shale gas is investigated through GCMC simulations. The recovery mechanisms and efficiencies of pressure drawdown and CO_2 injection are investigated. Our simulation results show that for the adsorption of methane, ethane and propane ternary mixtures in the kerogen slit pores, densities of methane and ethane in the first adsorption layer increase with increasing pressure, while that of propane displays an opposite trend. Larger confinement effect due to nanopores is observed on the heavier components due to stronger fluid-surface interactions. During the shale gas recovery process, propane in 2 nm kerogen slit pores can only be recovered by CO_2 injection, while pressure drawdown is able to recover propane from 4 nm kerogen slit pores but with low efficiency. Pressure drawdown and CO_2 injection take effect in different regions for different hydrocarbons: pressure drawdown recovers methane in the adsorption layer and middle of slit pores, while extracting ethane and propane mainly from the middle of slit pore; injected CO_2 mainly displaces hydrocarbons in the adsorption layer. Pressure drawdown tends to extract the lighter component and CO_2 injection is efficient in the recovery of heavier hydrocarbons. As pore width increases, the recovery ratio of pressure drawdown increases, while that of CO_2 injection decreases. Besides, the CO_2 sequestration ratio is higher in narrower kerogen slit pores.

As highlighted by Tesson and Firoozabadi [19], kerogen pore surface roughness may play an important role in hydrocarbon adsorption and recovery mechanism. In our future work, we would take into account such surface roughness to study hydrocarbon mixture adsorption and recovery in kerogen nanopores.

Acknowledgments

Support from the MOST National Key Research and Development Programme (Project No. 2016YFB0600805) and the Center for Combustion Energy at Tsinghua University is gratefully acknowledged. The simulations were partly performed on the High-Performance Parallel Computer supported by the Tsinghua HPC Platform. Additional support from the UK Engineering and Physical Sciences Research Council under the project UK Consortium on Mesoscale Engineering Sciences (UKCOMES) (Grant No. EP/R029598/1) is gratefully acknowledged. Z. J. acknowledges a Discovery Grant from Natural Sciences and Engineering Research Council of Canada (NSERC RGPIN-2017-05080).

References

[1] Vidic RD, Brantley SL, Vandenbossche JM, Yoxtheimer D, Abad JD. Impact of shale gas development on regional water quality. Science (80-) 2013;340:1235009. doi:10.1126/science.1235009.

[2] Melikoglu M. Shale gas: Analysis of its role in the global energy market. Renew Sustain

Energy Rev 2014;37:460–8. doi:10.1016/j.rser.2014.05.002.

[3] Kuuskraa VA, Stevens SH, Moodhe K. Technically Recoverable Shale Oil and Shale Gas Resources: An Assessment of 137 Shale Formations in 41 Countries Outside the United States. EIA 2013.

[4] Ehlinger VM, Gabriel KJ, Noureldin MMB, El-halwagi MM. Process Design and Integration of Shale Gas to Methanol. ACS Sustain Chem Eng 2014;2:30–37. doi:10.1021/sc400185b.

[5] He C, You F. Shale gas processing integrating with ethylene production : Novel process designs , exergy analysis , and techno-economic analysis. Ind Eng Chem Res 2014;53:11442–11459. doi:10.1021/ie5012245.

[6] Arogundade O, Sohrabi M. A Review of Recent Developments and Challenges in Shale Gas Recovery. SPE Saudi Arab Sect Tech Symp Exhib 2012:8–11. doi:10.2118/160869-MS.

[7] Bui K, Akkutlu IY. Hydrocarbons Recovery From Model-Kerogen Nanopores. SPE J 2017;22:854–62. doi:10.2118/185162-PA.

[8] Striolo A, Cole DR. Understanding Shale Gas: Recent Progress and Remaining Challenges. Energy and Fuels 2017;31:10300–10. doi:10.1021/acs.energyfuels.7b01023.

[9] Schepers KC, Nuttall BC, Oudinot AY, Gonazalez R. Reservoir Modeling and Simulation of the Devonian Gas Shale of Eastern Kentucky for Enhanced Gas Recovery and CO2 Storage. Soc Pet Eng 2009;126620-MS:1–20. doi:10.2118/126620-MS.

[10] Lackner KS. A Guide to CO2 Sequestration. Science (80-) 2003;300:1677–8. doi:10.1126/science.1079033.

[11] Ortiz Cancino OP, Peredo Mancilla D, Pozo M, Pérez E, Bessieres D. Effect of Organic Matter and Thermal Maturity on Methane Adsorption Capacity on Shales from the Middle Magdalena Valley Basin in Colombia. Energy and Fuels 2017;31:11698–709.

doi:10.1021/acs.energyfuels.7b01849.

[12] Wang T, Tian S, Li G, Sheng M, Ren W, Liu Q, et al. Molecular Simulation of CO2/CH4 Competitive Adsorption on Shale Kerogen for CO2 Sequestration and Enhanced Gas Recovery. J Phys Chem C 2018;122:17009–18. doi:10.1021/acs.jpcc.8b02061.

[13] Zhang H, Cao D. Molecular simulation of displacement of shale gas by carbon dioxide at different geological depths. Chem Eng Sci 2016;156:121–7. doi:10.1016/j.ces.2016.09.002.

[14] Sun H, Zhao H, Qi N, Li Y. Molecular Insights into the Enhanced Shale Gas Recovery by Carbon Dioxide in Kerogen Slit Nanopores. J Phys Chem C 2017;121:10233–41. doi:10.1021/acs.jpcc.7b02618.

[15] Huang L, Ning Z, Wang Q, Qi R, Zeng Y, Qin H, et al. Molecular simulation of adsorption behaviors of methane, carbon dioxide and their mixtures on kerogen: Effect of kerogen maturity and moisture content. Fuel 2018;211:159–72. doi:10.1016/j.fuel.2017.09.060.

[16] Sui H, Yao J. Effect of surface chemistry for CH4/CO2 adsorption in kerogen: A molecular simulation study. J Nat Gas Sci Eng 2016;31:738–46. doi:10.1016/j.jngse.2016.03.097.

[17] Zeng K, Jiang P, Lun Z, Xu R. Molecular Simulation of Carbon Dioxide and Methane Adsorption in Shale Organic Nanopores. Energy & Fuels 2019;33:1785–96. doi:10.1021/acs.energyfuels.8b02851.

[18] Zhou J, Jin Z, Luo KH. Effects of Moisture Contents on Shale Gas Recovery and CO2 Sequestration. Langmuir 2019;35:8716–25. doi:10.1021/acs.langmuir.9b00862.

[19] Tesson S, Firoozabadi A. Methane Adsorption and Self-Diffusion in Shale Kerogen and Slit Nanopores by Molecular Simulations. J Phys Chem C 2018:23528–42. doi:10.1021/acs.jpcc.8b07123.

[20] Zhou J, Mao Q, Luo KH. Effects of Moisture and Salinity on Methane Adsorption in

Kerogen: A Molecular Simulation Study. Energy & Fuels 2019;33:5368–76. doi:10.1021/acs.energyfuels.9b00392.

[21] Falk K, Pellenq R, Ulm FJ, Coasne B. Effect of Chain Length and Pore Accessibility on Alkane Adsorption in Kerogen. Energy and Fuels 2015;29:7889–96. doi:10.1021/acs.energyfuels.5b02015.

[22] Zhao H, Lai Z, Firoozabadi A. Sorption Hysteresis of Light Hydrocarbons and Carbon Dioxide in Shale and Kerogen. Sci Rep 2017;7:1–10. doi:10.1038/s41598-017-13123-7.

[23] Zhao H, Wu T, Firoozabadi A. High pressure sorption of various hydrocarbons and carbon dioxide in Kimmeridge Blackstone and isolated kerogen. Fuel 2018;224:412–23. doi:10.1016/j.fuel.2018.02.186.

[24] Wu T, Zhao H, Tesson S, Firoozabadi A. Absolute adsorption of light hydrocarbons and carbon dioxide in shale rock and isolated kerogen. Fuel 2019;235:855–67. doi:10.1016/j.fuel.2018.08.023.

[25] Wu H, He Y, Qiao R. Recovery of Multicomponent Shale Gas from Single Nanopores. Energy and Fuels 2017;31:7932–40. doi:10.1021/acs.energyfuels.7b01013.

[26] Chalmers GR, Bustin RM, Power IM. Characterization of gas shale pore systems by porosimetry, pycnometry, surface area, and field emission scanning electron microscopy/transmission electron microscopy image analyses: Examples from the Barnett, Woodford, Haynesville, Marcellus, and Doig uni. Am Assoc Pet Geol Bull 2012;96:1099–119. doi:10.1306/10171111052.

[27] Curtis ME, Cardott BJ, Sondergeld CH, Rai CS. Development of organic porosity in the Woodford Shale with increasing thermal maturity. Int J Coal Geol 2012;103:26–31. doi:10.1016/j.coal.2012.08.004.

[28] Tissot, B. P., Welte DH. Petroleum Formation and Occurrence. vol. 66. 1985. doi:10.1029/EO066i037p00643.

[29] Vandenbroucke M. Kerogen : from Types to Models of Chemical Structure. Oil Gas Sci Technol – Rev d'IFP Energies Nouv 2003;58:243–69. doi:10.2516/ogst:2003016.

[30] Jarvie DM, Hill RJ, Ruble TE, Pollastro RM. Unconventional shale-gas systems: The Mississippian Barnett Shale of north-central Texas as one model for thermogenic shale-gas assessment. Am Assoc Pet Geol Bull 2007;91:475–99. doi:10.1306/12190606068.

[31] Ungerer P, Collell J, Yiannourakou M. Molecular modeling of the volumetric and thermodynamic properties of kerogen: Influence of organic type and maturity. Energy and Fuels 2015;29:91–105. doi:10.1021/ef502154k.

[32] Kelemen SR, Afeworki M, Gorbaty ML, Sansone M, Kwiatek PJ, Walters CC, et al. Direct Characterization of Kerogen by X-ray and Solid-State 13C Nuclear Magnetic Resonance Methods. Energy and Fuels 2007;21:1548–61. doi:10.1021/ef060321h.

[33] Collell J, Ungerer P, Galliero G, Yiannourakou M, Montel F, Pujol M. Molecular simulation of bulk organic matter in type ii shales in the middle of the oil formation window. Energy and Fuels 2014;28:7457–66. doi:10.1021/ef5021632.

[34] Plimpton S. Fast Parallel Algorithms for Short-Range Molecular-Dynamics. J Comput Phys 1995;117:1–19. doi:10.1006/jcph.1995.1039.

[35] Mayo SL, Olafson BD, Goddard WA. DREIDING: a generic force field for molecular simulations. J Phys Chem 1990;94:8897–909. doi:10.1021/j100389a010.

[36] Shelley JC, Patey GN. Boundary condition effects in simulations of water confined between planar walls. Mol Phys 1996;88:385–98. doi:10.1080/00268979650026406.

[37] Zumberge J, Ferworn K, Brown S. Isotopic reversal ('rollover') in shale gases produced from

the Mississippian Barnett and Fayetteville formations. Mar Pet Geol 2012;31:43–52. doi:10.1016/j.marpetgeo.2011.06.009.

[38] Martin MG, Siepmann JI. Transferable Potentials for Phase Equilibria. 1. United-Atom Description of n-Alkanes. J PhysChem B 1998:2569–77. doi:10.1002/aic.15816.

[39] Lorentz HA. Ueber die Anwendung des Satzes vom Virial in der kinetischen Theorie der Gase. Ann Phys 1881;248:127–36. doi:10.1002/andp.18812480110.

[40] Frenkel D, Smit B. Understanding Molecular Simulation: From Algorithms to Applications. 2002.

[41] Van Der Ploeg P, Berendsen HJC. Molecular dynamics simulation of a bilayer membrane. J Chem Phys 1982;76:3271–6. doi:10.1063/1.443321.

[42] Potoff JJ, Siepmann JI. Vapor-liquid equilibria of mixtures containing alkanes, carbon dioxide, and nitrogen. AIChE J 2001;47:1676–82. doi:10.1002/aic.690470719.

[43] Martin MG. MCCCS Towhee : a tool for Monte Carlo molecular simulation. Mol Simul 2013;39:1212–1222. doi:10.1080/08927022.2013.828208.

[44] Widom B. Potential-Distribution Theory and the Statistical Mechanics of Flulds. J Phys Chem 1982;715:869–72. doi:10.1021/j100395a005.

[45] Widom B. Some Topics in the Theory of Fluids 1963;2808. doi:10.1063/1.1734110.

[46] Peng D, Robinson DB. A New Two-Constant Equation of State. Ind Eng Chem Fundam 1976;15:59–64. doi:10.1021/i160057a011.

[47] Lu L, Wang Q, Liu Y. Adsorption and Separation of Ternary and Quaternary Mixtures of Short Linear Alkanes in Zeolites by Molecular Simulation. Langmuir 2003;19:10617–10623. doi:10.1021/la034766z.

[48] Steele WA. The physical interaction of gases with crystalline solids. I. Gas-solid energies and

properties of isolated adsorbed atoms. Surf Sci 1973;36:317–52. doi:10.1016/0039-6028(73)90264-1.

[49] Denayer JFM, Daems I, Baron G V. Adsorption and Reaction in Confined Spaces. Oil Gas Sci Technol - Rev IFP 2006;61:561–9. doi:10.2516/ogst:2006025a.

[50] Yu W, Lashgari H, Sepehrnoori K. Simulation Study of CO2 Huff-n-Puff Process in Bakken Tight Oil Reservoirs. Soc Pet Eng 2014. doi:10.2118/169575-MS.

[51] Meng X, Meng Z, Ma J, Wang T. Performance Evaluation of CO 2 Huff-n-Puff Gas Injection in Shale Gas Condensate Reservoirs. Energies 2019;12:1–18. doi:10.3390/en12010042.

[52] Takbiri-Borujeni A, Kazemi M, Liu S, Zhong Z. Molecular simulation of enhanced oil recovery in shale. Energy Procedia 2019;158:6067–72. doi:10.1016/j.egypro.2019.01.510.

[53] Sun H, Zhao H, Qi N, Li Y. Simulation to Enhance Shale Gas Recovery Using Carbon Dioxide in Silica Nanopores with Different Sizes. Energy Technol 2017;5:2065–71. doi:10.1002/ente.201700166.

[54] Sun H, Zhao H, Qi N, Qi X, Zhang K, Li Y. Molecular insight into the micro-behaviors of CH4 and CO2 in montmorillonite slit-nanopores. Mol Simul 2017;43:1004–11. doi:10.1080/08927022.2017.1328553.